DNS AND EXPERIMENTS ON THERMAL CONVECTION IN STORAGE TUBES OF HYPERSONIC LUDWIEG FACILITIES

Jean-Marc Heinricy
Institute of Aerodynamics
RWTH Aachen University
52062 Aachen, Germany
jm.heinricy@aia.rwth-aachen.de

Léon Lüer
Institute of Fluid Mechanics
Technische Universität Braunschweig
38108 Braunschweig, Germany
leon.lueer@tu-braunschweig.de

Wolfgang Schröder
Institute of Aerodynamics
RWTH Aachen University
52062 Aachen, Germany
office@aia.rwth-aachen.de

Rolf Radespiel
Institute of Fluid Mechanics
Technische Universität Braunschweig
38108 Braunschweig, Germany
rolf.radespiel@tu-braunschweig.de

Dominik Krug
Institute of Aerodynamics
RWTH Aachen University
52062 Aachen, Germany
d.krug@aia.rwth-aachen.de

David Rival
Institute of Fluid Mechanics
Technische Universität Braunschweig
38108 Braunschweig, Germany
david.rival@tu-braunschweig.de

ABSTRACT

Flow inside a heated horizontal tube subjected to gravity is investigated under the Oberbeck-Boussinesq assumption using direct numerical simulations (DNS) based on a lattice Boltzmann method and experiments. A helical wall temperature distribution with pitch $\lambda/D = 1.15$ is considered, which is representative of many storage tubes of hypersonic wind tunnels of Ludwieg type. The Prandtl number is fixed to $\mathrm{Pr} = 0.70$ and Rayleigh numbers between $\mathrm{Ra} = 4.3 \cdot 10^7$ and $\mathrm{Ra} = 1.1 \cdot 10^9$ are considered, corresponding to the bounds of the operating range of the Hypersonic Ludwieg Tube Braunschweig (HLB) facility. For all Rayleigh numbers in this range, the flow is unsteady and chaotic throughout the system. Turbulence statistics are observed to vary considerably in all space dimensions. Furthermore, the wall temperature distribution causes convection rolls rotating in the azimuthal direction. Time traces of the temperature recorded using physical thermocouples confirm the main trends observed in the simulations.

INTRODUCTION

In hypersonic flight vehicle development, laminar-turbulent boundary layer transition is of critical importance, as it affects wall shear stress, surface heat flux, and flow separation (Schneider, 2004). In this context, transition is often studied in hypersonic Ludwieg tubes, which provide a cost-effective way of generating hypersonic, low-enthalpy flow. In such facilities, the test gas is first pressurized and heated inside a long cylindrical storage tube, then released through a fast-acting valve into a Laval nozzle, producing a short-duration hypersonic flow. A schematic of the HLB facility is shown in Fig. 1. The transition behavior observed in such experiments is inevitably influenced by freestream disturbances present in the test section, such that comparisons with numerical predictions, flight data, and other wind tunnel experiments (Schneider, 2001) are not straightforward. Consequently, quantifying these disturbances and reporting them alongside the results is necessary. Freestream disturbances in high-speed tunnels are typically described as a superposition of acoustic, entropy, and vorticity modes (Kovasznay, 1953). Acoustic disturbances mostly originate from the turbulent boundary layers on the inner walls of the nozzle. Entropy disturbances are caused by the heating of the fluid prior to conducting experiments, a measure necessary to prevent condensation of the test gas during expansion in the nozzle. Vorticity disturbances are mainly generated by mechanical installations, e.g., valves and struts. While acoustic modes have historically been considered to dominate over the other disturbance types (Morkovin, 1957), recent experiments by Munoz *et al.* (2019) cast doubt on this assumption. It was found that facilities with identical Laval nozzle geometries, but varying heating setups and storage tube lengths, yielded significantly different results regarding transition. This discrepancy is attributed to the entropy and vorticity perturbations originating upstream of the nozzle throat. For this reason, the startup process of hypersonic Ludwieg tubes has to be analyzed in greater detail.

In the present contribution, flow inside the storage tube of the HLB facility during the initial heating phase is investigated by means of DNS and physical thermocouples. This facility is representative of other hypersonic Ludwieg tubes and the findings presented hereafter can be transferred to similar wind tunnels. Ultimately, these insights are essential for determining realistic inflow boundary conditions at the nozzle throat for subsequent DNS of the Laval nozzle and test section, which are expected to provide conclusive insights into the influence of the heating process on transition experiments (Radespiel *et al.*, 2025).

This paper is organized as follows. First, the underlying flow problem is fully defined through specifying the flow geometry, boundary conditions, and dimensionless numbers. Next, an overview of the numerical and experimental setups used to generate the data is given. Then, general characteristics as well as specific aspects of the observed flow fields are discussed. Particular emphasis is placed on the influence of the Rayleigh number. Finally, the essential results are summarized and an outlook is given.

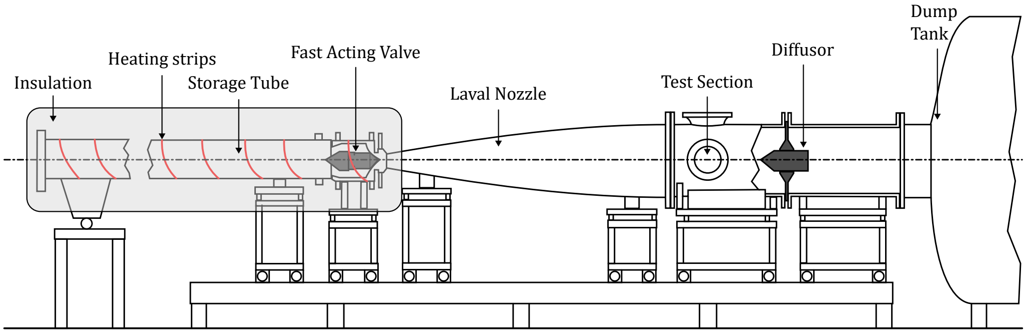

Figure 1: Design drawing of Hypersonic Ludwieg Tube Braunschweig (HLB) facility.

CASE SETUP

Flow Configuration

Figure 2 summarizes the geometry and boundary conditions used in the numerical simulations of the storage tube. The air inside the tube is heated to a mean temperature of $T_0 = 200\,^{\circ}\mathrm{C}$ by means of helically arranged heating strips. The energy provided by the heating strips eventually equals the heat losses to the ambient air, leading to a steady temperature field on the storage tube walls. The corresponding inhomogeneous wall temperature profile is approximated by

$$T = T_0 + \frac{\Delta T}{2}\cos(\frac{2\pi}{\lambda}x + \varphi - \varphi_0) \tag{1}$$

based on the results of a preliminary heat transfer simulation. In this equation, $\Delta T = T_{\mathrm{max}} - T_{\mathrm{min}}$ is the temperature difference between the maximum and minimum temperature on the inner wall, λ is the pitch of the helix, φ is the azimuthal angle defined in Fig. 2, and φ_0 is a reference angle introduced for generality. For the HLB, $\lambda/D = 1.15$, where $D = 0.27\,\mathrm{m}$ is the inner diameter, and $\Delta T = 20\,\mathrm{K}$. This temperature profile is assumed to be unaffected by the flow inside the storage tube, i.e., a one-way coupling between the wall temperature distribution and the flow is assumed for the purposes of the present work.

Aside from the helix pitch, the thermal convection flow is determined by the Rayleigh number $\mathrm{Ra} = \beta \Delta T g D^3/\nu\kappa$ and the Prandtl number $\mathrm{Pr} = \nu/\kappa$, where β is the thermal expansion coefficient, g denotes the gravity, ν is the kinematic viscosity, and κ is the thermal diffusivity. The unit Reynolds number Re_{m} inside the test section is controlled via the stagnation pressure p_0 inside the storage tube, which can be varied in the range between 3 and 15 bar. Assuming validity of the ideal gas equation, this results in a Prandtl number of $\mathrm{Pr} = 0.70$, and Rayleigh numbers $\mathrm{Ra} \in [4.3 \cdot 10^7,\, 1.1 \cdot 10^9]$ according to the thermodynamic data from Kadoya *et al.* (1985). The present contribution focuses on the three representative operating points of $p_0 \in \{3, 7, 15\}$ bar, corresponding to unit Reynolds numbers of $\mathrm{Re}_{\mathrm{m}} \in \{2.5 \cdot 10^6, 5.9 \cdot 10^6, 1.3 \cdot 10^7\}$ m^{-1} and Rayleigh numbers of $\mathrm{Ra} \in \{4.3 \cdot 10^7, 2.3 \cdot 10^8, 1.1 \cdot 10^9\}$. The relation between p_0 and Re_m is estimated from previous measurements (Radespiel *et al.*, 2016). Throughout this paper, all quantities are non-dimensionalized using the free-fall velocity $\sqrt{\beta \Delta T g D}$, the diameter D, and the temperature difference ΔT. The origin O of the Cartesian coordinate system is on the cylinder axis at the center of the computational domain, see Fig. 2.

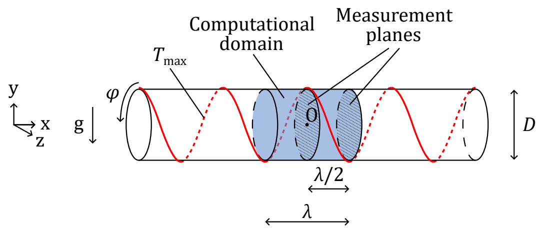

Figure 2: Storage tube geometry, heating strip layout, computational domain and positions of experimental measurement planes.

Numerical Method

The flow is simulated using a thermal lattice Boltzmann method (LBM) (Guo *et al.*, 2007) of the multi-physics solver m-AIA (multi-physics – Aerodynamisches Institut Aachen) (RWTH Aachen University, 2024). This particular LBM makes use of the Oberbeck-Boussinesq approximation, which is applicable in the context of the present flow according to the criteria from Gray & Giorgini (1976). The corresponding form of the conservation equations is

$$\nabla \cdot \vec{u} = 0 \tag{2}$$

$$\frac{\partial \vec{u}}{\partial t} + (\vec{u} \cdot \nabla)\vec{u} = -\frac{1}{\rho}\nabla p + \nu \nabla^2 \vec{u} - \beta (T - T_0)\vec{g} \tag{3}$$

$$\frac{\partial T}{\partial t} + (\vec{u} \cdot \nabla) T = \kappa \nabla^2 T \tag{4}$$

where $\vec{u}$ is the velocity vector, ρ is density, p is static pressure and t is time. The periodicity of the boundary conditions is exploited and only a segment with a length of one pitch is simulated, as shown in Fig. 2. The variable temperature boundary condition is applied using the boundary treatment by Li *et al.* (2014) and the local grid refinement technique proposed by Eitel-Amor *et al.* (2013) is used. Simulations are started from a uniform temperature field with $T = T_0$. The flow is given 75 free-fall times $D/\sqrt{\beta \Delta T g D}$ to reach a statistically steady state. Time integration for statistics is then performed over a further 75 free-fall times. Recorded time signals have a resolution of 200 samples per free-fall time, whereas the time resolution of the simulation corresponds to 20000 time steps per free-fall time. Simulations were carried out on a locally refined Cartesian mesh. Cells closest to the wall have a size of $D/2400$, cells inside the bulk have a size of $D/600$. Lastly, in the present lattice Boltzmann model, there is one additional degree of freedom in the form of the ratio of the free-fall velocity and the constant speed of sound a_0. Low values provide

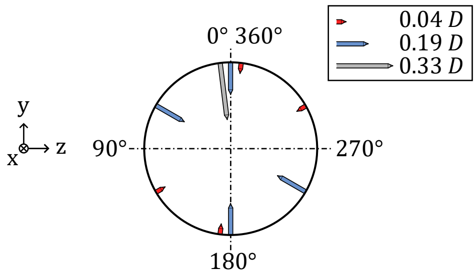

Figure 3: Thermocouple arrangement within the measurement planes.

better accuracy, while larger values lead to larger time steps and thus shorter simulation times. In the present study, the ratio $\sqrt{\beta \Delta T g D}/a_0 = 0.2$ was used.

Experimental Setup

Figure 2 shows the position of the two experimental measurement planes in the storage tube relative to the heating strip layout. The planes are spaced by half a helical pitch ($\lambda/2$), such that in one plane, the helical heating strip lies at $\varphi = 0°/360°$ (top), while in the other, it lies at $\varphi = 180°$ (bottom), where natural convection effects are expected to be most pronounced due to the local mean temperature gradient opposing gravity. Figure 3 shows the detailed arrangement of thermocouples in the measurement planes. In each plane, 9 Type K thermocouples with a sheath diameter of 0.25 mm are installed and arranged to resolve temperature fluctuations both close to the wall and in the bulk flow. The nominal response time of the thermocouples is 7.5 ms, measured for a step change in water. However, the effective response time in air is expected to be higher due to the lower convective heat transfer.

RESULTS AND DISCUSSION

Resolution Requirements

To the best of the authors' knowledge, the present physical problem does not correspond to any canonical test case in the literature. Therefore, no a priori knowledge of the required spatial resolution was available. Instead, progressively finer meshes were used until the variation in the observed quantities was negligible. At $\mathrm{Ra} = 1.1 \cdot 10^9$, the validity of the Kolmogorov hypotheses is expected at least locally. While a detailed investigation of the Kolmogorov scaling will be addressed in future research, the mesh resolution is related to the Kolmogorov length scale in this section.

At $\mathrm{Pr} < 1$, the Kolmogorov length $\eta = (\nu^3/\varepsilon_u)^{1/4}$, where ε_u is the turbulent dissipation, is an often used measure for the resolution requirements of DNS. Following Stevens *et al.* (2010), the grid must satisfy $h \leq \pi\eta$, with $h = \max(\Delta x, \Delta y, \Delta z)$. For the lattice Boltzmann scheme used in the present study, a Cartesian grid is used, i.e., the extent of the cells is the same in all Cartesian directions. Turbulent dissipation is found to be highest at the outer walls beneath the convection rolls in Fig. 10.

Figure 4 shows the Kolmogorov length scale at $\mathrm{Ra} = 1.1 \cdot 10^9$ across a vertical line at $(x = \lambda/4, z = 0)$. The resolution requirements are highest close to the walls and slightly less restrictive in the bulk. The current mesh resolution used for the present study yields values of $h/\eta \approx 10$. While not quite meeting the criterion cited above, the resolution seems appropriate for the present analysis.

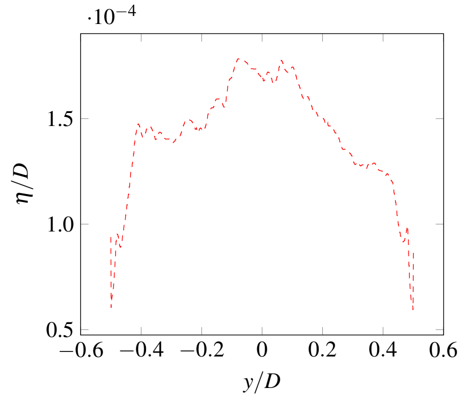

Figure 4: Kolmogorov length η as a function of vertical coordinate y at $x = \lambda/4$ and $z = 0$ at $\mathrm{Ra} = 1.1 \cdot 10^9$.

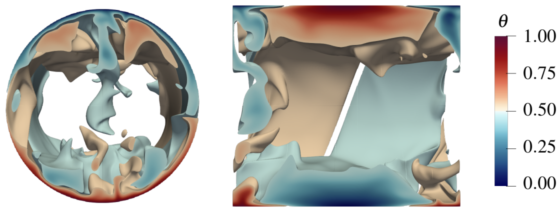

(a) y-z-plane (b) x-z-plane

Figure 5: Contours of instantaneous temperature difference in $\theta \in [0.0, 0.45] \cup [0.55, 1.0]$ at $\mathrm{Ra} = 4.3 \cdot 10^7$.

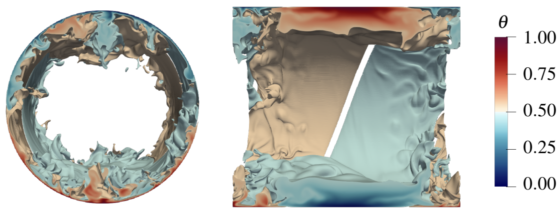

(a) y-z-plane (b) x-z-plane

Figure 6: Contours of instantaneous temperature difference in $\theta \in [0.0, 0.45] \cup [0.55, 1.0]$ at $\mathrm{Ra} = 1.1 \cdot 10^9$.

Instantaneous Flow Characteristics

Figures 5 and 6 show contours of the non-dimensionalized instantaneous temperature difference $\theta = (T - T_{\min})/\Delta T$ in the range $\theta \in [0.0, 0.45] \cup [0.55, 1.0]$ at Rayleigh numbers of $4.3 \cdot 10^7$ and $1.1 \cdot 10^9$. Throughout the entire operating range of the HLB, the flow inside the storage tube is unsteady and chaotic. As the Rayleigh number increases, the bulk of the total temperature difference is found in increasingly thin regions close to the wall. Plumes are observed near the axial locations $x = \pm\lambda/2$, where the heating strip is located at the bottom of the tube and the local mean temperature gradient of the wall acts against gravity. At higher Rayleigh numbers, the flow exhibits progressively small-scale structures, with plumes becoming thinner and more spatially refined.

Figure 7 shows the simulated time trace of the temperature difference θ starting from an arbitrary time t_0 at position $(\lambda/2, 0.46D, 0)$, corresponding to the upper thermocouple located closest to the wall in Fig. 3. Fluctuations become increasingly fast at higher Rayleigh numbers, as evidenced by the larger number of local minima and maxima at

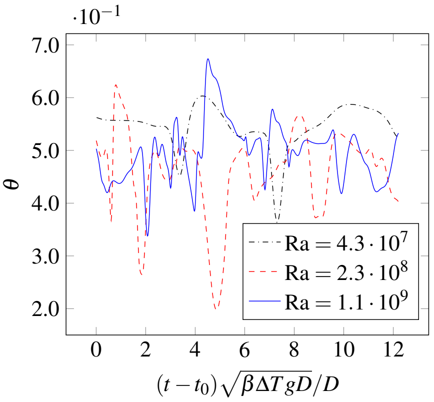

Figure 7: Simulated time signal of temperature difference θ at position $(\lambda/2, 0.46D, 0)$.

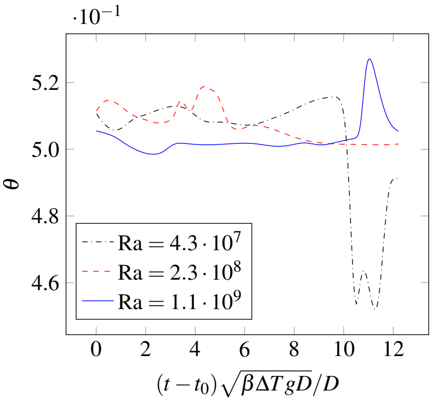

Figure 8: Simulated time signal of temperature difference θ at position $(\lambda/2, 0.17D, 0)$.

Table 1: Reynolds number Re_φ of maximum mean azimuthal velocity as a function of the Rayleigh number.

Ra	$4.3 \cdot 10^7$	$2.3 \cdot 10^8$	$1.1 \cdot 10^9$
Re_φ	2084	4633	10880

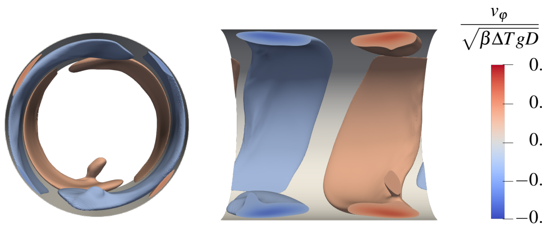

(a) y-z-plane (b) x-z-plane

Figure 9: Contours of mean azimuthal velocity in interval $v_\varphi/\sqrt{\beta \Delta T g D} \in [-0.22, -0.07] \cup [0.07, 0.22]$ at $\mathrm{Ra} = 4.3 \cdot 10^7$.

(a) y-z-plane (b) x-z-plane

Figure 10: Contours of mean azimuthal velocity in interval $v_\varphi/\sqrt{\beta \Delta T g D} \in [-0.22, -0.07] \cup [0.07, 0.22]$ at $\mathrm{Ra} = 1.1 \cdot 10^9$.

$\mathrm{Ra} = 1.1 \cdot 10^9$ compared to $\mathrm{Ra} = 2.3 \cdot 10^8$ and $\mathrm{Ra} = 4.3 \cdot 10^7$. Even at $\mathrm{Ra} = 1.1 \cdot 10^9$, the time span between neighboring local extrema generally remains on the order of one free-fall time and thus well above the time resolution used for sampling. For all Rayleigh numbers considered, temperature fluctuations above $0.2\Delta T$ are observed at this location.

Figure 8 shows the simulated temperature signal at position $(\lambda/2, 0.17D, 0)$, corresponding to the upper thermocouple located furthest from the wall in Fig. 3. For all Rayleigh numbers, the amplitude of the observed temperature fluctuations is smaller at this location compared to regions closer to the wall. The peaks in Fig. 8 are due to plumes occasionally reaching this far into the bulk. Without these events, fluctuations are comparatively slow and have a low amplitude.

Mean Flow Characteristics

Time averaged velocities reveal coherent flow structures. Figures 9 and 10 show contours of the mean azimuthal velocity v_φ in the range $v_\varphi/\sqrt{\beta \Delta T g D} \in [-0.22, -0.07] \cup [0.07, 0.22]$. Two counterrotating convection rolls are observed close to the outer walls, generating shear stresses in the near wall regions. Figure 11 shows the mean azimuthal velocity profile along the vertical y-axis at $(x = \lambda/4, z = 0)$. The mean azimuthal velocity profiles are approximately symmetric around $y = 0$ with distinct peaks close to the walls. The higher the Rayleigh number, the closer the peaks move to the wall. For the Reynolds number $\mathrm{Re}_\varphi = \max(|v_\varphi|)D/\nu$ based on the maximum mean azimuthal velocity, the values in Table 1 are obtained. For the three Rayleigh numbers shown, Re_φ increases roughly proportionally to $\mathrm{Ra}^{0.5}$, which is a direct consequence of $\max(|v_\varphi|)/\sqrt{\beta \Delta T g D}$ being approximately constant across all Rayleigh numbers.

To quantify the amplitudes of the unsteady motions at different locations of the computational domain, the spatial distribution of the turbulent kinetic energy (TKE) $k = \frac{1}{2}\langle(u'^2 + v'^2 + w'^2)\rangle$ is considered, where u', v' and w' are the velocity fluctuations in Cartesian directions. Figures 12, 13, and 14 show the distributions of the cross-sectional, azimuthal, and meridional means of TKE respectively. The corresponding definitions are

$$k_x(x) = \frac{4}{\pi D^2} \int_0^{2\pi} \int_0^{D/2} k(x, \varphi, r)\, r \,\mathrm{d}r \,\mathrm{d}\varphi \tag{5}$$

$$k_r(r) = \frac{1}{2\pi\lambda} \int_0^{2\pi} \int_{-\lambda/2}^{\lambda/2} k(x, \varphi, r) \,\mathrm{d}x \,\mathrm{d}\varphi \tag{6}$$

$$k_\varphi(\varphi) = \frac{2}{D\lambda} \int_0^{D/2} \int_{-\lambda/2}^{\lambda/2} k(x, \varphi, r) \,\mathrm{d}x \,\mathrm{d}r \tag{7}$$

Figure 12 shows that for all Rayleigh numbers, TKE is minimal in the plane at $x = 0$ where the heating strip is located at the top of the pipe. TKE is maximal in the plane at $x = \lambda/2$, where the heating strip is located at the bottom of the pipe. Figure 13 quantifies the radial distribution of TKE. At $\mathrm{Ra} = 4.3 \cdot 10^7$ and $\mathrm{Ra} = 2.3 \cdot 10^8$, TKE is distributed close to equally across all radii. In contrast, at $\mathrm{Ra} = 1.1 \cdot 10^9$, the regions located further away from the central axis show higher levels of TKE

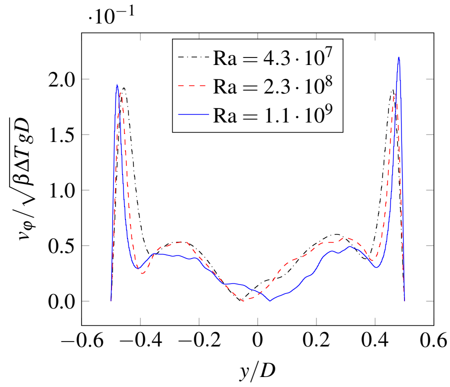

Figure 11: Mean azimuthal velocity profile as a function of the vertical coordinate y at $x = \lambda/4$ and $z = 0$.

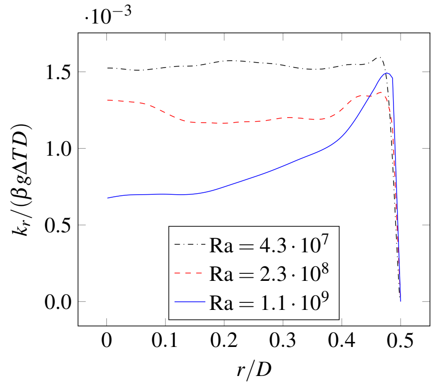

Figure 13: Azimuthal average of TKE as a function of the distance r to the cylinder axis.

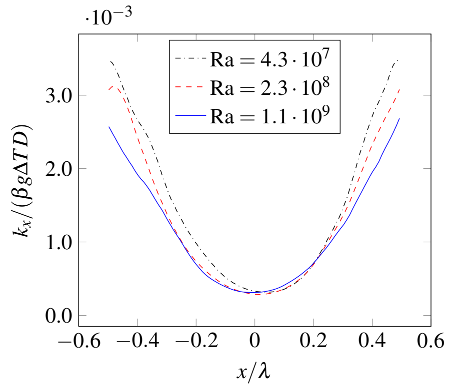

Figure 12: Cross-sectional average of TKE as a function of the axial position x.

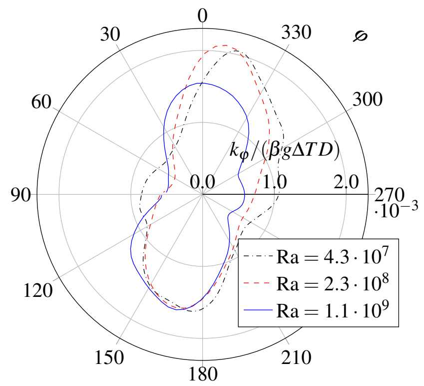

Figure 14: Meridional average of TKE as a function of the azimuthal angle φ.

than the regions close to the central axis. Figure 14 quantifies the distribution of TKE to different azimuthal directions. For all Rayleigh numbers, inhomogeneity is observed, with higher levels of TKE in the vertical directions $\varphi = 0°$ and $\varphi = 180°$ than in the horizontal directions $\varphi = 90°$ and $270°$.

At increasing Rayleigh number, the volume average of TKE over the whole system is found to decrease slightly. This is evident in Fig. 12, which shows that the cross-sectional averages of TKE decrease with increasing Rayleigh number for virtually all axial positions. Figure 13 indicates that the decrease in total TKE occurs in the bulk rather than in the near-wall regions. Figure 14 reveals that the largest decrease in TKE is observed at $\varphi = 0°$, i.e., in the direction opposing gravity. A possible explanation of this result is that as the Rayleigh number increases, TKE is redistributed from the bulk toward finer structures close to the outer walls. Future research will clarify this point by focusing on the TKE budget in relevant regions of the system at different Rayleigh numbers.

Experimental Measurements

Figures 15 and 16 show the measured time traces of the temperature difference θ starting from an arbitrary time t_0 at the positions $(\lambda/2, 0.46D, 0)$ and $(\lambda/2, 0.17D, 0)$ respectively. Thus, the signals correspond to those shown in Figs. 7 and 8. Importantly, the definition of θ is slightly altered in the sense that it is computed based on the maximum temperature difference ΔT and minimum temperature T_{min} measured across all probes at a given pressure. This change was made, since the maximum and minimum temperatures at the inner wall are not measurable in the present setup.

The measurements confirm some of the trends observed in the simulations. For one, with increasing pressure, i.e., increasing Rayleigh number, the fluctuations become increasingly fast and their amplitudes increase noticeably beyond a critical value of Ra. This trend is most obvious in Fig. 15, where temperature differences of approximately $0.05\Delta T$ are observed at the two higher pressures, whereas the amplitude of the fluctuations is smaller than $0.01\Delta T$ for the lowest pressure. For another, fluctuations are most pronounced close to the walls. Even at the highest pressure of $p_0 = 15\,\mathrm{bar}$, fluctuations do not exceed $0.02\Delta T$ in Fig. 16.

However, there are important discrepancies between the numerical and experimental time traces, both in the observed amplitudes, time scales and mean temperature levels. These differences are attributed to several uncertainties. First, the experiments yielded larger maximum temperature differences of $\Delta T = 50\,\mathrm{K}$ and a lower mean temperature level of $T_0 = 160\,°\mathrm{C}$ than assumed in the simulations. For this reason, the Rayleigh numbers used in the simulations do not exactly correspond to those at the corresponding pressures in the experiments. Second, there is uncertainty regarding the axial position of the measurement positions relative to the heating spiral and thus the exact match of the positions of the physical and numerical probes. Third, due to imperfections in the insulation of the storage tube as well as modifications made to get measuring access, there is uncertainty regarding the match of the assumed and actual wall temperature distributions. These uncertainties will be further investigated in future research.

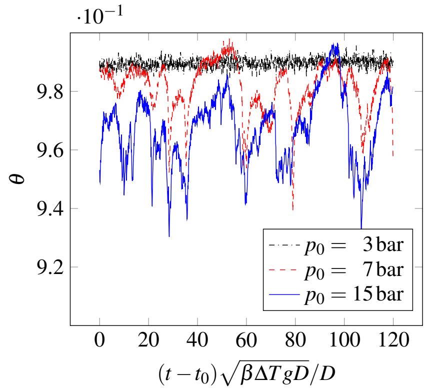

Figure 15: Measured time signal of temperature difference θ at position $(\lambda/2, 0.46D, 0)$.

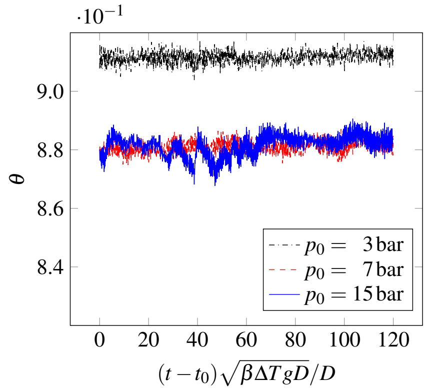

Figure 16: Measured time signal of temperature difference θ at position $(\lambda/2, 0.17D, 0)$.

CONCLUSIONS AND OUTLOOK

The flow regime inside horizontal storage tubes of hypersonic Ludwieg facilites during the initial heating face is investigated using DNS and measurements. A helical temperature profile is assumed in the simulations based on the heating setup of the HLB facility. It is found that the Rayleigh numbers at typical operating conditions are sufficiently high to cause unsteady and chaotic flow throughout the system. Turbulence statistics are highly inhomogeneous and depend on the local disposition of the helical heating strip relative to the gravity vector. In planes where the heating strip is located at the bottom of the tube, TKE is highest and plume shedding is the most pronounced. Outside of the locations where the heating strip is located at the bottom of the tube, thermal stratification is observed. Aside from turbulent fluctuations, two convection rolls rotating in the azimuthal direction are observed in the mean velocity field. With increasing Rayleigh number, the Reynolds number based on the maximum azimuthal velocity of the convection rolls increases roughly proportionally to $\mathrm{Ra}^{0.5}$.

In addition to the simulations, time traces of the temperature were recorded experimentally at several representative points. The experiments confirm the main trends that the fluctuations become increasingly fast with increasing pressure. Furthermore, the experiments show that fluctuations are most pronounced close to the walls, as predicted by the simulations. However, an exact match between simulations and experiments is not obtained due to various uncertainties.

Future studies will focus on the TKE budget to clarify the mechanism responsible for the observed decrease of the total TKE contained in the system with increasing Rayleigh number. Furthermore, heat transfer from the hotter parts of the wall to the colder parts will be quantified to judge whether the assumption of one-way coupling between the wall temperature distribution and the flow field is justified in simulations. Additional physical probes will be used to get additional insights into the wall temperature distribution and allow more accurate modeling of the wall temperature distribution in simulations.

ACKNOWLEDGMENTS

This work was supported by the Deutsche Forschungsgemeinschaft (DFG), grant 520690340. Computational resources were provided by the High Performance Computing Center of the University of Stuttgart (HLRS).

REFERENCES

Eitel-Amor, G., Meinke, M. & Schröder, W. 2013 A lattice-boltzmann method with hierarchically refined meshes. *Computers & Fluids* **75**, 127–139.

Gray, D. D. & Giorgini, A. 1976 The validity of the boussinesq approximation for liquids and gases. *International Journal of Heat and Mass Transfer* **19** (5), 545–551.

Guo, Z., Zheng, C., Shi, B. & Zhao, T. S. 2007 Thermal lattice Boltzmann equation for low Mach number flows: Decoupling model. *Physical Review E* **75** (3), 036704.

Kadoya, K., Matsunaga, N. & Nagashima, A. 1985 Viscosity and thermal conductivity of dry air in the gaseous phase. *Journal of Physical and Chemical Reference Data* **14** (4), 947–970.

Kovasznay, L. S. G. 1953 Turbulence in supersonic flow. *Journal of the Aeronautical Sciences* **20** (10), 657–674.

Li, L., Mei, R. & Klausner, J. F. 2014 Heat transfer evaluation on curved boundaries in thermal lattice boltzmann equation method. *Journal of Heat Transfer* **136** (1), 012403.

Morkovin, M. V. 1957 On transition experiments at moderate supersonic speeds. *Journal of the Aeronautical Sciences* **24** (7), 480–486.

Munoz, F., Ali, S. R. C., Leinemann, M., Radespiel, R., Semper, M., Cummings, R. & Theiss, A. 2019 Transition measurements on slender and blunt bodies in Ludwieg tubes at Mach 6. In *AIAA SciTech 2019 Forum*. American Institute of Aeronautics and Astronautics.

Radespiel, R., Estorf, M., Heitmann, D., Muñoz, F. & Wolf, T. 2016 Hypersonic ludwieg tube. In *Experimental Methods of Shock Wave Research* (ed. O. Igra & F. Seiler), pp. 433–458. Springer International Publishing.

Radespiel, R., Rosi, G. A., Soy, K., Rival, D. E., Heinricy, J.-M. & Schröder, W. 2025 Inverse decomposition method for complete determination of freestream disturbances in a hypersonic wind tunnel. In *AIAA SciTech 2025 Forum*. American Institute of Aeronautics and Astronautics.

RWTH Aachen University 2024 m-AIA. Zenodo, doi:10.5281/zenodo.13350586.

Schneider, S. P. 2001 Effects of high-speed tunnel noise on laminar-turbulent transition. *Journal of Spacecraft and Rockets* **38** (3), 323–333.

Schneider, S. P. 2004 Hypersonic laminar–turbulent transition on circular cones and scramjet forebodies. *Progress in Aerospace Sciences* **40** (1-2), 1–50.

Stevens, R. J. A. M., Verzicco, R. & Lohse, D. 2010 Radial boundary layer structure and nusselt number in rayleigh–bénard convection. *Journal of fluid mechanics* **643**, 495–507.